Dynamic Recrystallisation Pathways Governing Creep-Induced Microstructural Evolution in Additively Manufactured Inconel 718

P.E. May[1], M. White[2], A. Bordin[2], L. Ednie[2], R. Huff[3], T. Abdullah[1], S. Vunnam[4], L. Becker[5] and R.J. Lancaster[1]*

[1] Swansea University, Institute of Structural Materials, Bay Campus, Fabian Way, Swansea, SA1 8EN, United Kingdom
[2] ASTM International UK Ltd, Bristol, UK
[3] ASTM International, Washington, DC, USA
[4] swathivunnam@gmail.com
[5] AddUp Solution Center, 5101 Creek Rd, Cincinnati, OH 45242, USA
* Corresponding author: r.j.lancaster@swansea.ac.uk; +44 1792 295965

Abstract

Understanding how creep deformation alters microstructure is critical for assessing the long-term stability of high-temperature alloys. This study investigates creep-induced microstructural evolution in Inconel 718 (IN718) produced by laser beam powder bed fusion (PBF-LB), through the use of electron backscatter diffraction (EBSD). Constant-load creep tests were conducted at 625-675 °C and 625-690 MPa on vertically built material subjected to two post-processing heat treatments designed to produce contrasting grain boundary and dislocation structures. EBSD-based analysis of grain boundary character, recrystallisation fraction, twin density and geometrically necessary dislocation (GND) density, before and after creep exposure shows that creep stability is governed by the dominant dynamic recrystallisation (DRX) pathway activated during deformation. A high-temperature solution plus double ageing treatment promotes deformation-dominated DRX, characterised by sustained GND accumulation, stable low-angle boundary networks and controlled twin evolution, resulting in creep resistance comparable to wrought IN718. In contrast, a lower-temperature heat treatment exhibits recovery-dominated behaviour, with GND annihilation, increased high-angle boundary formation and accelerated damage accumulation. By treating creep as a driver of microstructural evolution, this study demonstrates the value of EBSD-derived metrics for identifying active deformation pathways and provides mechanistic insight into the microstructural design of IN718 for high-temperature service.

Keywords: laser beam powder bed fusion; IN718; creep; dynamic recrystallisation

1. Introduction

Additive manufacturing (AM) of metallic alloys has enabled unprecedented geometric complexity and design freedom for high-temperature components, but it also introduces microstructural features that differ fundamentally from those produced by conventional processing routes [1], [2]. In precipitation-hardened nickel-based superalloys such as Inconel 718 (IN718), laser beam powder bed fusion (PBF-LB) produces non-equilibrium microstructures characterised by fine cellular substructures, residual dislocation networks, crystallographic texture and elemental segregation [3], [4]. These features can be beneficial for ambient-temperature strength but often compromise microstructural stability under prolonged high-temperature loading, where creep deformation becomes the dominant life-limiting mechanism [5]–[7].

The high-temperature performance of IN718 is governed by the stability of its microstructure, including the γ''/γ' precipitation state, grain boundary character, dislocation substructure and the distribution of secondary phases such as carbides and δ phase [5]–[7]. In additively manufactured IN718, post-processing heat treatments are therefore essential to mitigate as-built heterogeneities, dissolve detrimental phases and promote microstructural configurations suitable for long-term service [8]–[11]. Numerous studies have shown that appropriate solution and ageing treatments can substantially improve creep rupture life in PBF-LB IN718; however, these improvements are often rationalised primarily in terms of grain size or static phase content [9], [11], [12].

A growing body of evidence indicates that creep deformation in IN718 is accompanied by significant microstructural evolution, including dynamic recrystallisation (DRX), grain boundary transformation and the rearrangement of dislocations [13], [14]. Rather than acting as a purely time-dependent deformation process, creep in IN718 involves continuous interactions between dislocation activity, grain boundary migration and phase stability, which together govern strain accommodation and damage accumulation at elevated temperature. These microstructural processes are particularly important in precipitation-hardened superalloys, where the stability of dislocation substructures and grain boundaries strongly influences resistance to tertiary creep and rupture.

In wrought IN718, both continuous and discontinuous DRX mechanisms have been reported under creep and hot-deformation conditions, influencing strain accommodation and damage accumulation [13], [15], [16]. Continuous DRX is typically associated with progressive subgrain rotation driven by dislocation accumulation and recovery, leading to gradual increases in boundary misorientation. Discontinuous DRX, by contrast, involves the nucleation and growth of new, strain-free grains at existing high-angle grain boundaries or twin intersections, often contributing to localised grain refinement. These DRX mechanisms have been shown to influence creep response by modifying grain boundary character distributions, redistributing dislocation density and altering the pathways available for strain localisation and cavity formation.

By comparison, the manifestation of DRX during creep in additively manufactured IN718 remains considerably less well understood. Laser beam powder bed fusion (PBF-LB) produces microstructures that differ fundamentally from wrought material, including fine cellular substructures, non-equilibrium solute segregation, high residual dislocation densities and complex grain boundary networks inherited from rapid solidification and cyclic thermal exposure during processing [17], [18]. These features can either promote or suppress DRX during subsequent high-temperature deformation, depending on their stability and interaction with post-processing heat treatments. Moreover, post-processing can substantially modify the as-built microstructure by dissolving segregated phases, promoting recrystallisation and altering grain boundary character, complicating direct comparisons with wrought behaviour.

Despite increasing interest in the creep performance of additively manufactured IN718, most existing studies have focused on rupture life, minimum creep rate or comparisons between different processing routes, often correlating performance with static microstructural features such as grain size, texture or precipitate distribution [9], [19], [20]. While these metrics provide valuable benchmarks, they offer limited insight into the dynamic microstructural processes that govern long-term stability during creep. In particular, relatively little attention has been paid to how microstructures evolve during creep exposure and how this evolution differs between additively manufactured and wrought material.

This paper will now investigate how contrasting post-processing heat treatments influence and control the dominant dynamic recrystallisation pathway during creep in additively manufactured IN718, and how this pathway governs tertiary creep stability. The present study hypothesises that creep resistance in PBF-LB IN718 is governed not primarily by grain size or precipitate state, but by whether the microstructure evolves through a deformation-dominated DRX pathway (characterised by sustained GND accumulation and stable LAGB networks) or a recovery-dominated pathway (characterised by dislocation annihilation and boundary coarsening). The objective of this work is therefore to establish quantitative EBSD-based metrics capable of discriminating between these pathways and linking them directly to macroscopic creep behaviour.

2. Experimental Methods

2.1. Material and Processing

Cylindrical creep specimens of IN718 were fabricated by PBF-LB using gas-atomised powder in an argon atmosphere. Gas atomisation and PBF-LB processing routes for IN718 are known to introduce rapid solidification microstructures, residual dislocation networks and microsegregation that necessitate

post-processing heat treatment [1], [2], [4]. Figure 1 presents representative scanning electron microscopy (SEM) images of the gas-atomised IN718 powder used for PBF-LB processing. All specimens were manufactured in the vertical (90 °) orientation to reflect conditions commonly investigated in prior creep studies of additively manufactured IN718 [8], [9]. The powder size distribution (PSD) was characterised by D_{10}, D_{50}, and D_{90} values of 5.2 µm, 10.63 µm, and 17.25 µm, respectively. The specimens were built on a FormUp 350 system operating in an inert argon atmosphere. The machine parameters, pre-set by the manufacturer, resulted in a volumetric energy density of 44.44 J/mm³.

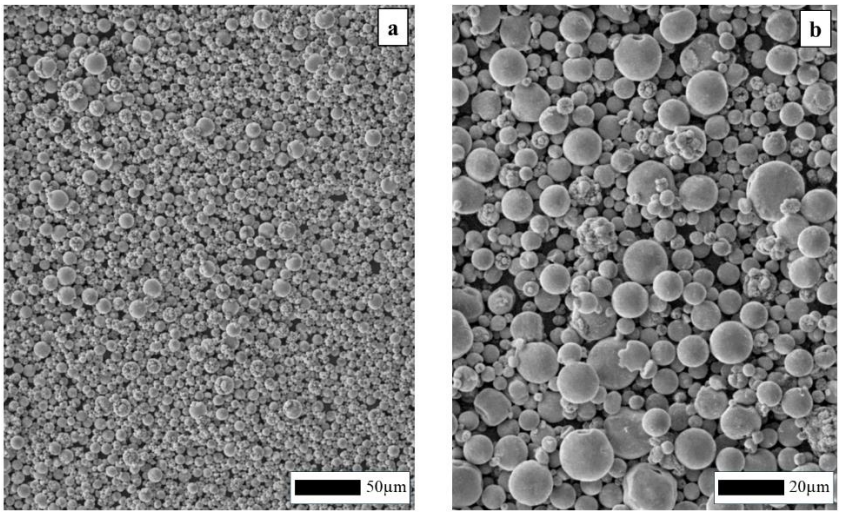

Figure 1. SEM images of gas-atomised IN718 powder used for laser powder bed fusion: **a)** low magnification showing particle morphology and size distribution, and **b)** higher magnification highlighting predominantly spherical particles with limited satellite formation.

Following fabrication, samples were either retained in the as-received (AR) condition or subjected to one of two post-processing heat treatments designed to produce contrasting grain boundary and precipitate states. Heat treatment 1 (HT1) comprised solution annealing at 1065 °C for 1 h followed by controlled cooling and a two-stage ageing treatment, consistent with high-temperature homogenisation strategies reported to improve creep resistance [11], [17], [22]. Heat treatment 2 (HT2) employed a lower-temperature solution treatment at 955 °C followed by a reduced-temperature double ageing schedule, representative of sub-solvus processing routes known to retain δ phase and finer grains [12], [23], [24]. Both heat treatments are presented schematically in Figure 2.

Wrought IN718, sourced from a commercial supplier, was solution annealed at 965 °C for 1 h prior to testing and served as a benchmark material, consistent with established processing routes for creep-resistant wrought IN718 [5].

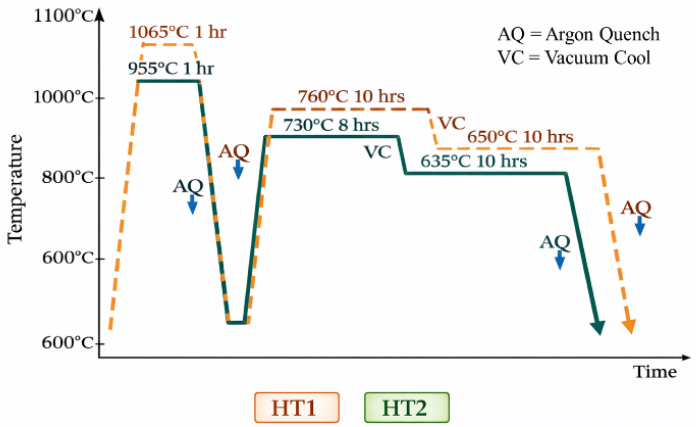

Figure 2. Heat treatment processing routes for HT1 and HT2.

2.2. Constant-Load Creep Testing

Constant-load creep tests were conducted in accordance with ASTM E139, which provides standardised guidance for high-temperature creep and creep-rupture testing of metallic materials[25]. Tests were performed at temperatures between 625 and 675 °C under applied stresses of 625-690 MPa, conditions representative of prior creep studies on wrought and additively manufactured IN718 [8], [9], [19]. Specimens were soaked at the test temperature for 1 h prior to load application to ensure thermal stabilisation. All creep tests were conducted under uniaxial constant-load tensile conditions in accordance with ASTM E139 [25]. Specimens were loaded in tension along the build direction (Z-axis), and strain was monitored continuously via high-temperature extensometry. No compressive creep testing was performed. Temperature was controlled using a radiant furnace and monitored by dual type R thermocouples positioned near the specimen gauge section, maintaining a tolerance of ±4 °C throughout testing, in line with established experimental practice [25].

2.3. Microstructural Characterisation

Electron backscatter diffraction (EBSD) was employed to characterise grain structure, grain boundary character, recrystallisation fraction and geometrically necessary dislocation (GND) density before and after creep testing. EBSD is widely used to quantify deformation-induced microstructural evolution, including DRX and dislocation storage, in IN718 and related superalloys [13], [15].

EBSD scans were performed under fixed conditions: aperture 1, 20 mm working distance, 20 kV accelerating voltage, spot size 100, 0.31 μm step size, and 4×4 binning, with phase set to 'Ni Superalloy'. Data was processed in HKL Tango Channel 5 with noise reduction applied to minimise zero solutions. Grain reconstruction used a minimum grain size of 10 pixels and a critical misorientation angle >10 ° with 2 % completion. Recrystallised grains were identified based on grain orientation spread thresholds, following approaches reported in the literature [14], [26]. Twin density was quantified as the length fraction of Σ3 boundaries relative to the total grain boundary length, consistent with established grain boundary character distribution analyses [15], [16]. GND density was calculated from local lattice curvature using established methods that relate orientation gradients to dislocation content [13], [14]. All post-creep EBSD analyses were conducted at comparable distances from the fracture surface to minimise spatial bias, as recommended in prior creep-microstructure studies [13], [15].

3. Results

3.1. Material

Figure 3 presents the microstructures of PBF-LB and wrought IN718. The PBF-LB samples display anisotropic features, with columnar grains in the XZ plane and finer equiaxed grains in the XY plane, while the wrought material, shown only in the XY plane, is isotropic with larger equiaxed grains. Relatively weak <100> texture was observed in the PBF-LB variants (MUD < 3.0). The wrought sample shows a significantly higher twin density (51.4 %) than all PBF-LB variants, with HT1 having the highest among them (21.5 %). HT2 exhibits smaller grains than AR and HT1 but retains some anisotropy between planes. As shown previously [27], the wrought material contains large carbides and finely dispersed δ phase. AR shows a continuous Laves network, while HT1 presents a refined γ matrix with dispersed carbides, δ, and Laves phases. HT2 shows an increased presence of grain boundary carbides, δ, and Laves. γ′ and γ″ phases are more readily identifiable in HT1 and HT2. Further information on the microstructural constituents and grain size metrics for the IN718 variants is documented in [27].

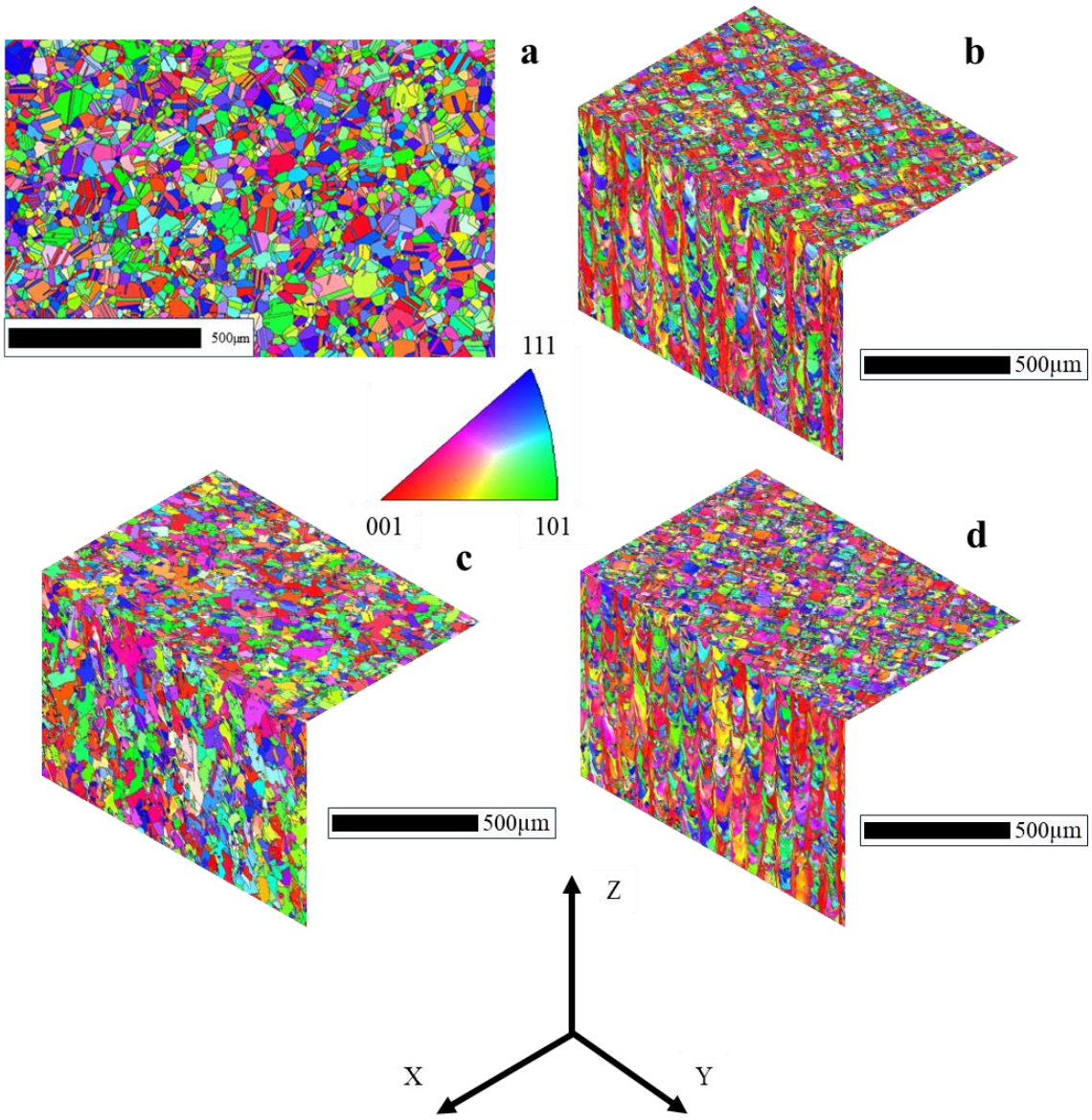

Figure 3: EBSD inverse pole figure maps of **a)** wrought, **b)** PBF-LB AR, **c)** PBF-LB HT1 and **d)** PBF-LB HT2 IN718.

3.2. Creep Behaviour

Constant-load creep curves obtained for wrought IN718 tested at a fixed stress of 650 MPa over a temperature range of 625-675 °C are shown in Figure 4. As shown, increasing temperature leads to a systematic acceleration of creep deformation, manifested by higher minimum creep rates and reduced rupture lives. This behaviour is consistent with enhanced dislocation mobility and thermally activated recovery processes at elevated temperature in precipitation-hardened nickel-based superalloys [6], [7], [28].

In addition to rupture life and minimum creep rate, the shape of the creep curves for wrought IN718 provides insight into the deformation processes active under the investigated conditions. Increasing temperature leads to a systematic reduction in primary creep duration and an earlier onset of strain-rate acceleration associated with tertiary creep, consistent with enhanced dislocation mobility and thermally activated recovery processes at elevated temperature. Such trends are well established for precipitation-hardened nickel-based superalloys and reflect the progressive loss of microstructural stability under sustained high-temperature loading [5]–[7].

The onset of tertiary creep was defined as the point at which the strain rate began to accelerate monotonically following the minimum creep rate, corresponding to the inflection in the creep curve where damage accumulation becomes dominant. This transition is associated with the progressive coalescence of grain boundary cavities and localised strain concentration, consistent with established creep behaviour in precipitation-hardened nickel-based superalloys [5–7, 28].

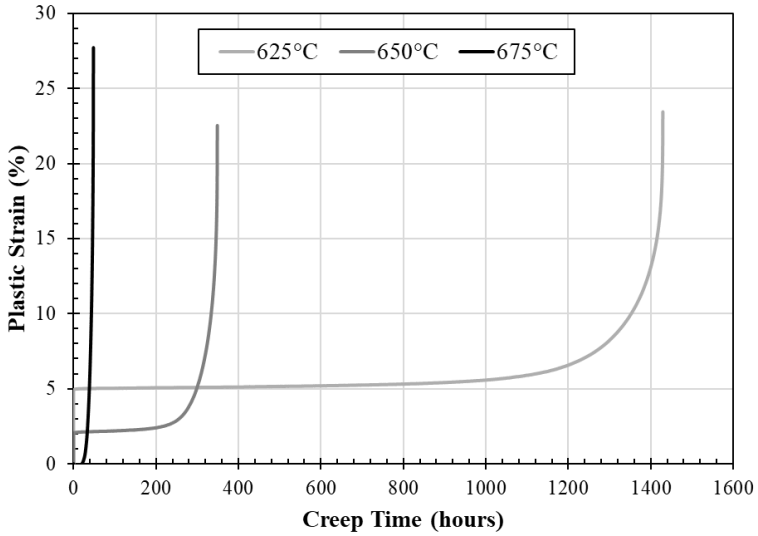

Figure 4. Constant-load creep curves for wrought IN718 tested at 650 MPa over a temperature range of 625-675 °C.

At a constant temperature of 650 °C, comparisons between wrought and PBF-LB variants reveal that wrought IN718 and the HT1 condition exhibit substantially longer rupture lives and lower minimum creep rates than the AR and HT2 conditions (Figure 5), indicating clear differences in creep stability between the PBF-LB variants and the wrought material. Similar trends have been reported for both wrought and additively manufactured IN718, where an appropriate heat treatment can significantly narrow the performance gap between AM and conventionally processed materials [8], [9], [11], [12]. The observed variations in creep stability therefore suggest that the additively manufactured materials exhibit distinct deformation responses under creep loading, motivating a detailed examination of creep-induced microstructural evolution.

In the stress and temperature range investigated here, creep deformation in IN718 is expected to be governed primarily by dislocation-controlled (power-law) creep rather than diffusional mechanisms [28]. As a result, differences in creep behaviour are most reasonably attributed to microstructural features that influence dislocation storage, recovery kinetics and grain boundary stability during creep exposure, rather than to grain size effects alone [13], [15]. Furthermore, although grain size varies across the investigated material variants, the observed creep behaviour cannot be rationalised solely on the basis of grain size. Notably, the HT1 condition exhibits creep resistance comparable to wrought IN718 despite a smaller average grain size, whereas HT2 shows inferior performance despite similar or larger grains than the AR condition. This indicates that creep behaviour under the present conditions is governed primarily by microstructural stability during deformation rather than static grain size effects alone [13], [15]. Consequently, differences in creep response are interpreted in terms of microstructural features that influence dislocation storage, recovery kinetics and grain boundary sliding resistance, including boundary character, precipitate distribution and dynamic recrystallisation behaviour [13], [15], [23]. Detailed results of all creep tests are presented in Table 1.

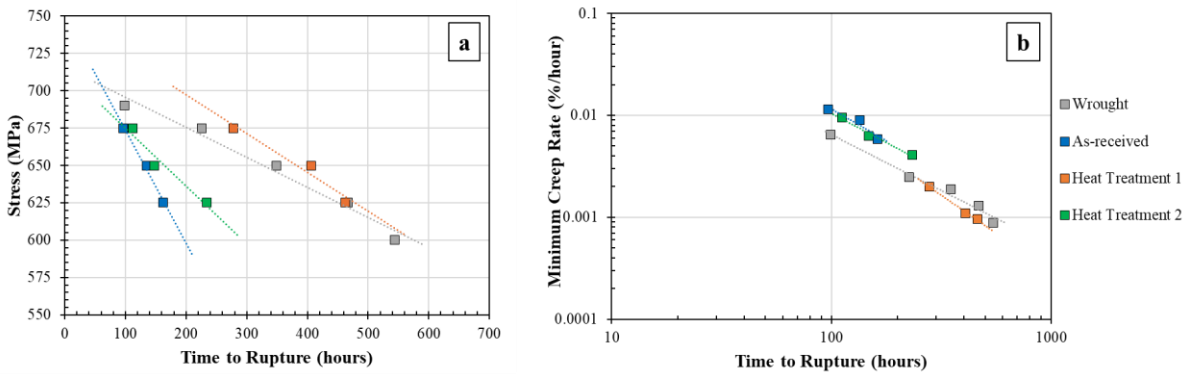

Figure 5. Comparison of creep performance for wrought and PBF-LB IN718 at 650 °C: **a)** time to rupture and **b)** minimum creep rate.

Table 1: Creep results for wrought and PBF-LB IN718 variants.

Material	Temp (°C)	Stress (MPa)	Time to Rupture (hours)	Minimum Creep Rate (%.hour^{-1})
Wrought	650	600	544	8.8×10^{-4}
	650	625	467	1.29×10^{-3}
	650	650	349	1.89×10^{-3}
	650	675	225	2.46×10^{-3}
	650	690	99	6.48×10^{-3}
	625	650	1429	3.1×10^{-4}
	675	650	48	1.45×10^{-2}
PBF-LB AR	650	625	162	5.83×10^{-3}
	650	650	134.8	9×10^{-3}
	650	675	96.7	1.15×10^{-2}
PBF-LB HT 1	650	625	462.7	9.69×10^{-3}
	650	650	405.7	1.09×10^{-3}
	650	675	278.4	2.01×10^{-3}
PBF-LB HT 2	650	625	233.7	4.07×10^{-3}
	650	650	147.2	6.3×10^{-3}
	650	675	112	9.52×10^{-3}

3.3. Microstructural Evolution During Creep

3.3.1. Wrought IN718

EBSD inverse pole figure (IPF) maps of wrought IN718 in the untested and creep tested conditions are shown in Figure 6. The untested material exhibits large equiaxed grains with a high fraction of annealing twins, consistent with a fully recrystallised wrought microstructure [5], [6]. Following creep exposure, pronounced grain refinement is observed alongside an increase in low-angle grain boundary (LAGB) fraction and a reduction in twin density. The full microstructural measurements are presented in Table 2.

The evolution of special grain boundaries in wrought IN718 is shown in Figure 7. The substantial reduction in Σ3 twin boundary fraction after creep indicates progressive twin degradation or transformation during sustained deformation. Similar twin breakdown during creep has been reported previously in IN718 and has been linked to the initiation of dynamic recrystallisation through boundary instability and stress concentration at twin–grain boundary intersections [13], [15], [16].

The apparent reduction in twin boundary density observed after creep exposure indicates that annealing twins are not microstructurally stable under sustained high-temperature loading. Twin degradation

during creep has been associated with stress concentration at twin-grain boundary intersections, which can promote boundary migration and act as preferential sites for recrystallisation nucleation [8]–[10]. The concurrent increase in low-angle boundary fraction and GND density suggests that creep deformation in wrought IN718 proceeds through a combination of continuous DRX, driven by subgrain rotation, and localised discontinuous DRX at high-angle boundary regions. These mechanisms collectively contribute to grain refinement and redistribution of strain during creep deformation.

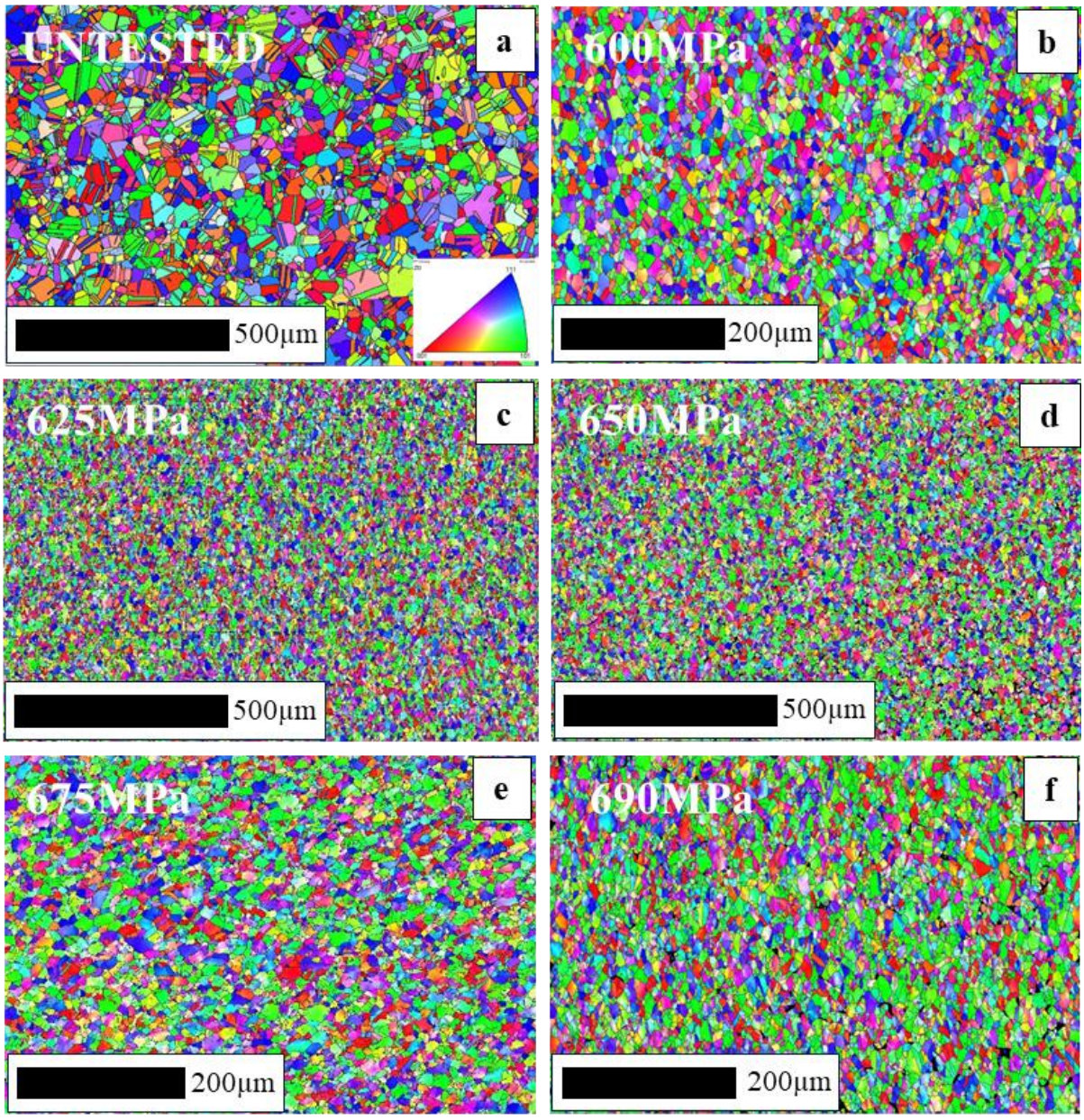

Figure 6. EBSD IPF maps of wrought IN718: **a)** untested condition and **b)-f)** specimens tested under constant-load creep at 600-690 MPa and 650 °C. All post-creep EBSD analyses were performed at comparable distances from the fracture surface to ensure consistency.

Table 2: Data from EBSD IPF maps for wrought IN718 before and after constant-load creep testing at 650 °C for 600-690 MPa. Rx = recrystallisation, HAGB = high angle grain boundaries, LAGB = low angle grain boundaries, MOS = mean orientation spread and GND = geometrically necessary dislocations.

Sample (Applied Load)	With Twins			Twin Density (%)	Rx (%)	HAGBs (%)	LAGBs (%)	MOS (°)	GND Density ($10^{14}/m^{-2}$)
	Grain Area ($\mu m^{2)}$	Grain Diameter (µm)	Aspect Ratio						
Untested	193	12.5	0.49	51.4	97.9	93.0	7.0	1.15	0.68
600MPa	44	6.3	0.56	4.32	33.6	21.9	78.1	4.9	2.98
625MPa	32	5.3	0.54	5.66	19.1	26.0	74.0	5.6	3.21
650MPa	43	6.2	0.56	4.88	25.6	23.0	77.0	4.5	3.08
675MPa	37	5.9	0.64	3.56	20.7	22.6	77.4	4.4	3.40
690MPa	31	5.3	0.56	2.44	17.6	17.4	82.6	5.2	3.40

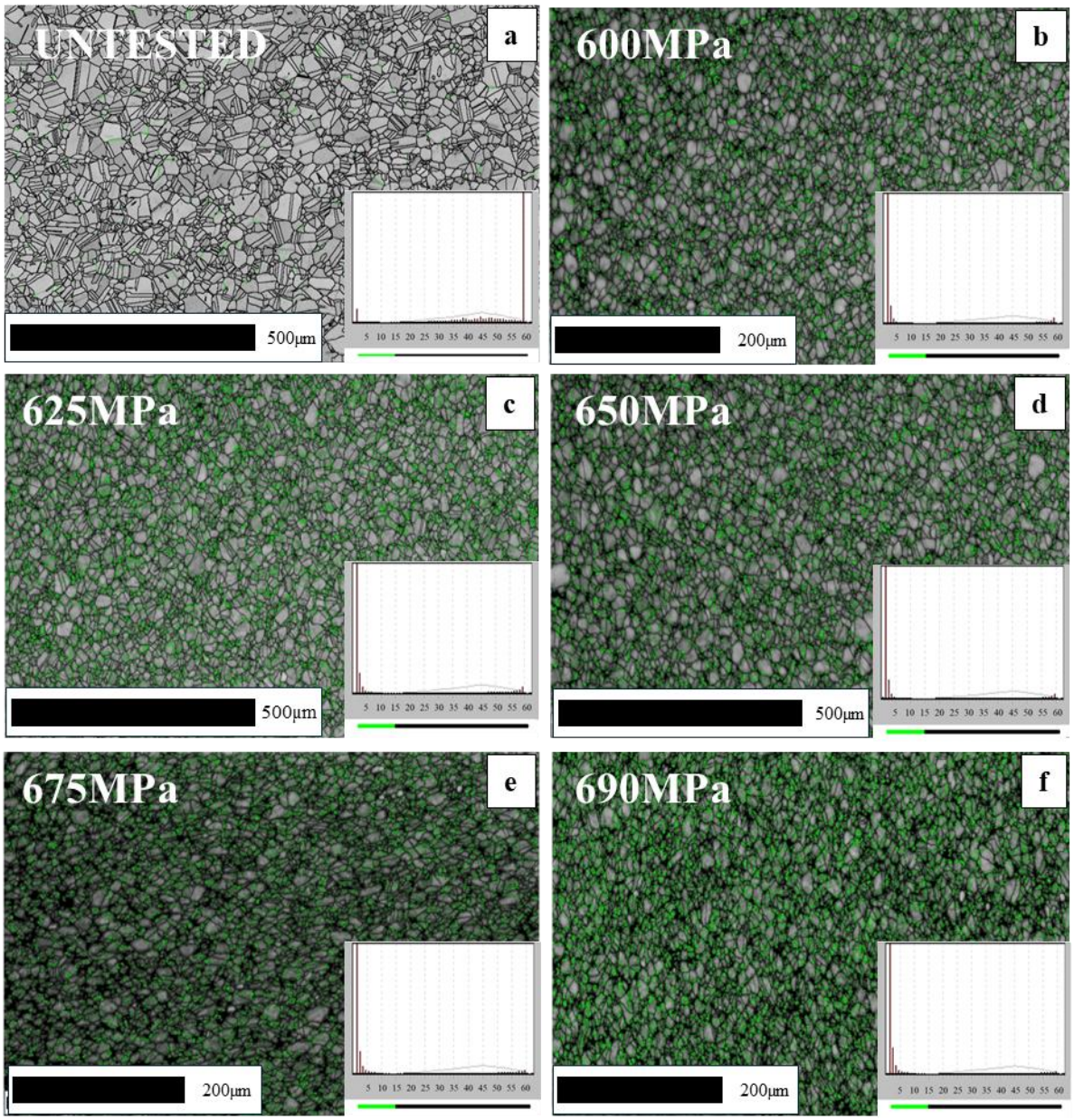

Figure 7. Distribution of special grain boundaries in wrought IN718 identified by EBSD, with Σ3 twin boundaries and related coincident site lattice (CSL) boundaries highlighted. Maps correspond to **a)** untested material and **b)–f)** specimens creep tested at 600-690 MPa. Twin density is quantified as the length fraction of Σ3 boundaries relative to the total grain boundary length; visual contrast does not directly represent boundary fraction due to projection and thresholding effects.

Another factor to consider is the geometrically necessary dislocation (GND) behaviour. GND maps have been produced through EBSD to provide a visual representation of local misorientation within the different IN718 variants and illustrative means of displaying the spatial distribution and density of GNDs across the different samples. The weighted mean GND density values are presented in Table 2, and were calculated using Eq. (1):

$$\overline{\rho}_{GND} = \frac{\Sigma(\rho_i \cdot f_i)}{\Sigma f_i} \quad (1)$$

Where ρ_i is GND density bin and f_i is the percentage (or fraction) in that bin.

The weighted mean GND density values provide a physically meaningful measure of the overall lattice curvature and stored plastic strain within the microstructure. GND density maps for wrought IN718 are presented in Figure 8. Post-creep specimens exhibit a marked increase in GND density, reflecting the accumulation of lattice curvature required to accommodate heterogeneous plastic deformation. Elevated GND densities are characteristic of deformation-dominated microstructures and provide strong evidence for active DRX during creep [13], [14].

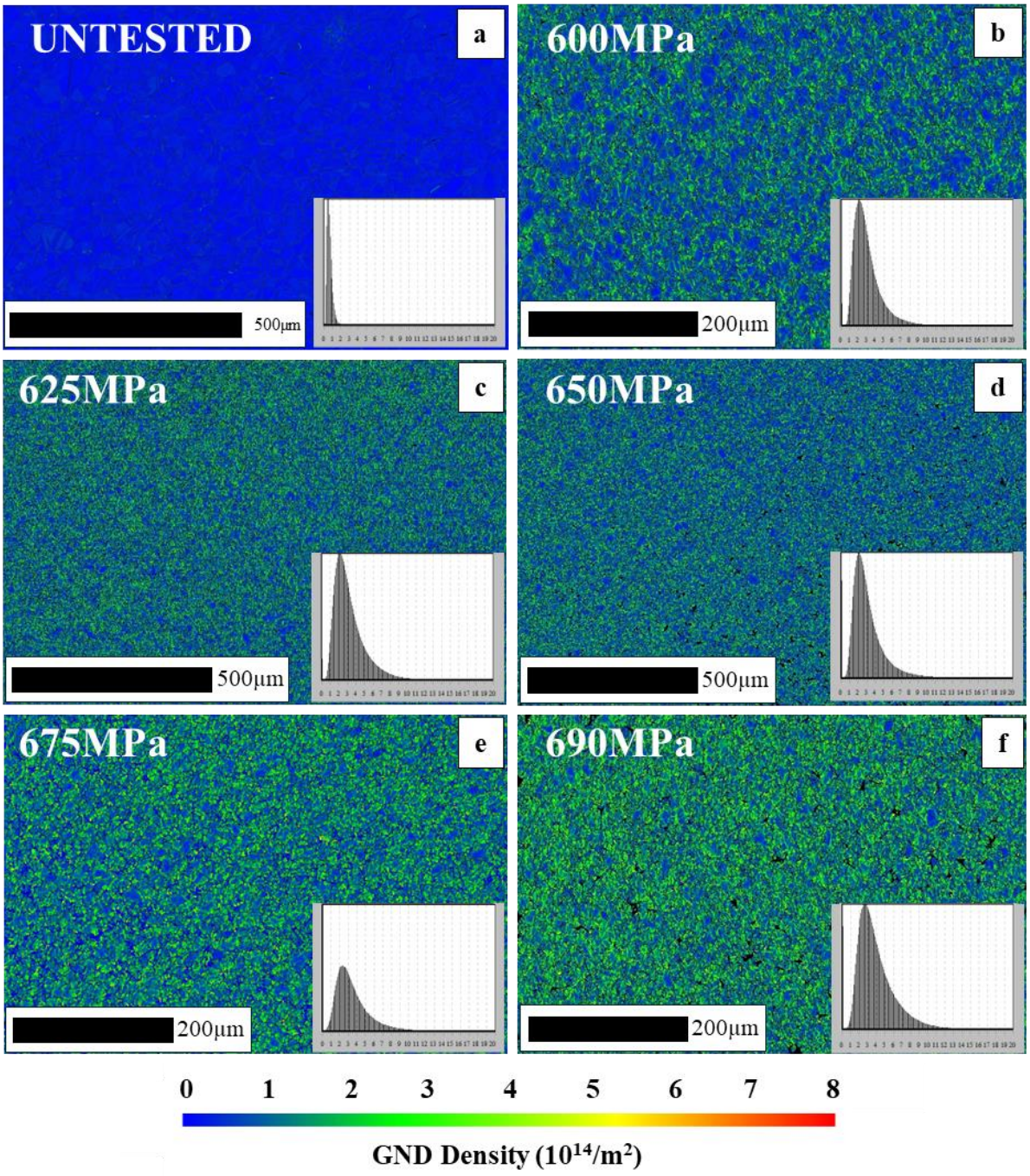

Figure 8. EBSD-derived geometrically necessary dislocation (GND) density maps for wrought IN718: **a)** untested and **b)-f)** tested at 600-690 MPa and 650 °C.

The GND maps show that the untested wrought material exhibits an expectedly low weighted mean GND density (~0.68×10^{14} m^{-2}), indicating a relatively relaxed dislocation structure. This is consistent with a microstructure dominated by statistically stored dislocations with limited long-range lattice curvature. The low GND content suggests minimal prior plastic incompatibility between grains, as

expected for an undeformed or lightly processed wrought condition. In contrast, the wrought material post creep testing shows a marked increase in weighted mean GND density, generally increasing with an increase in applied stress (~$3.2x10^{14}$ m^{-2} on average). This significant increase reflects substantial accumulation of GNDs during deformation, arising from strain gradients imposed by grain-to-grain mechanical incompatibility and the activation of heterogeneous slip systems. Therefore, once a critical plastic deformation regime is reached, the microstructure evolves toward a similarly high density of geometrically necessary dislocations. This behaviour is characteristic of wrought alloys, where relatively equiaxed grains and strong crystallographic constraints promote significant lattice curvature during deformation [5], [6].

3.3.2. PBF-LB Variants

EBSD IPF maps of wrought and PBF-LB variants in the untested and creep tested conditions are compared in Figure 9. All samples were subjected to the same test conditions (650 °C and 650 MPa). As shown, the AR condition displays a heterogeneous grain structure with a low initial twin density, reflecting the non-equilibrium solidification and residual strain introduced during the PBF-LB process [1]–[4].

Following creep exposure, both AR and HT1 exhibit increases in LAGB fraction and GND density, indicating deformation-driven microstructural evolution. In contrast, HT2 shows limited GND accumulation and a relative increase in high-angle grain boundary (HAGB) fraction, suggesting a dominant recovery-driven response. Similar contrasts between deformation- and recovery-dominated behaviour have previously been reported in AM IN718 subjected to different post-processing routes [12], [13], [21].

The evolution of GND density in the PBF-LB variants is further illustrated in Figure 10. HT1 exhibits a pronounced increase in GND density after creep, consistent with sustained dislocation storage and subgrain formation. Therefore, this condition displays characteristics consistent with deformation-dominated behaviour, including sustained GND accumulation and the retention of stable low-angle boundary networks. This suggests that the microstructure remains mechanically active throughout creep deformation, enabling strain accommodation without extensive boundary migration.

Conversely, HT2 shows a reduction in GND density, which can be attributed to enhanced dislocation annihilation, subgrain coarsening and boundary migration during creep, indicative of recovery-dominated behaviour [14], [26]. Enhanced recovery and boundary migration under these conditions are likely to promote grain boundary sliding and cavitation, reducing resistance to tertiary creep. Similar distinctions between deformation- and recovery-dominated creep behaviour have been reported in IN718 subjected to different thermomechanical histories and heat treatment strategies [12], [15], [21].

The full microstructural measurements for the PBF-LB variants are detailed in Table 3.

It is important to emphasise that under constant-load creep conditions the microstructure does not evolve toward a steady state but instead continuously adapts to the accumulating strain. The comparison between HT1 and HT2 therefore does not represent two static microstructures subjected to identical creep conditions, but rather two distinct evolutionary trajectories during deformation. HT1 sustains dislocation storage and subgrain rotation, promoting a deformation-dominated DRX pathway that stabilises boundary networks and delays damage localisation. In contrast, HT2 exhibits enhanced recovery and boundary migration, leading to reduced lattice curvature, increased high-angle boundary formation and accelerated cavitation. Therefore the microstructures do not simply differ after creep, but post-processing heat treatments bias the dominant creep-evolution pathway, which in turn governs the onset of tertiary creep and rupture life.

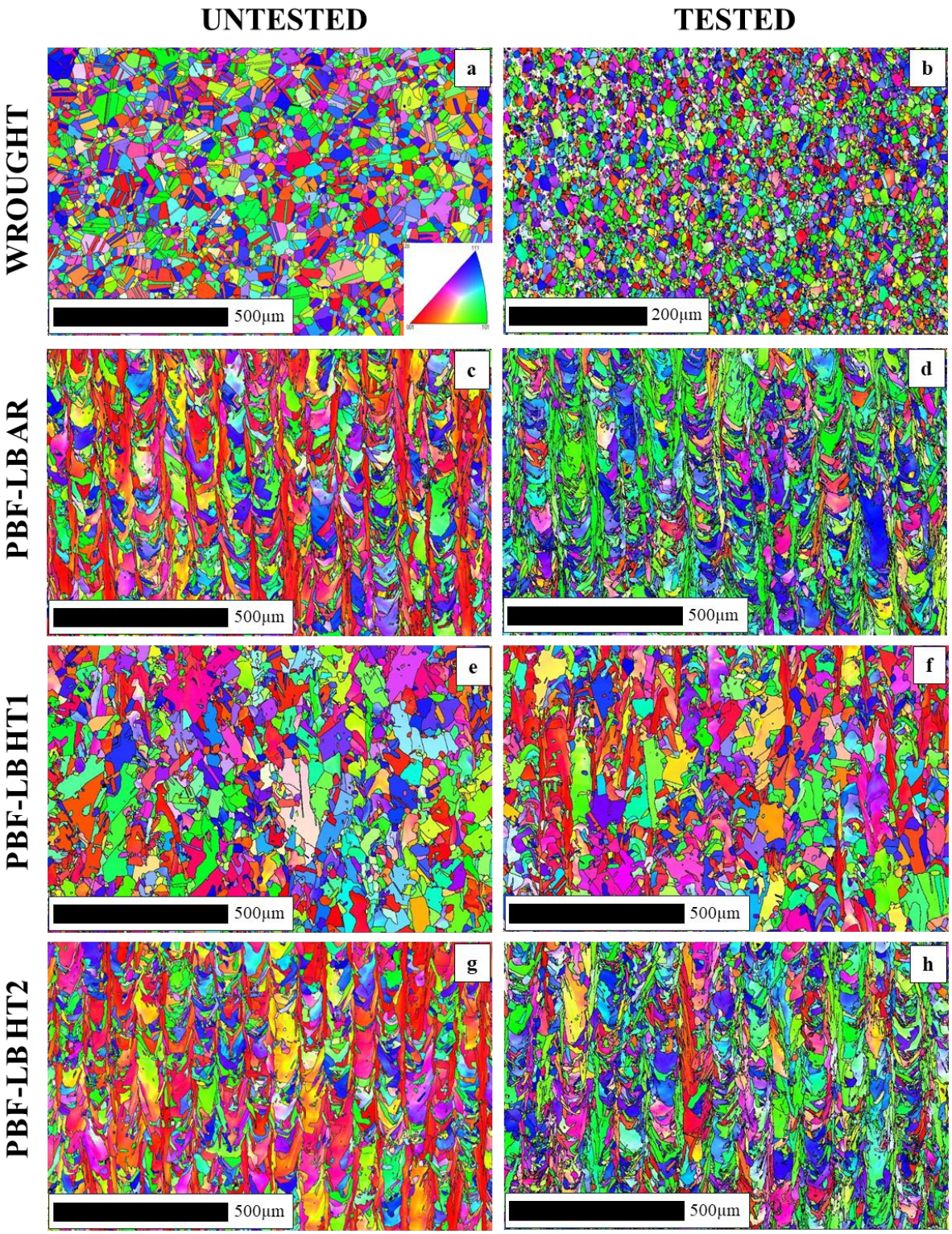

Figure 9. EBSD IPF maps of untested and creep tested specimens for wrought and PBF-LB IN718 variants, showing microstructural evolution induced by creep deformation at 650 °C and 650 MPa. All maps correspond to the X–Z plane (parallel to the loading direction).

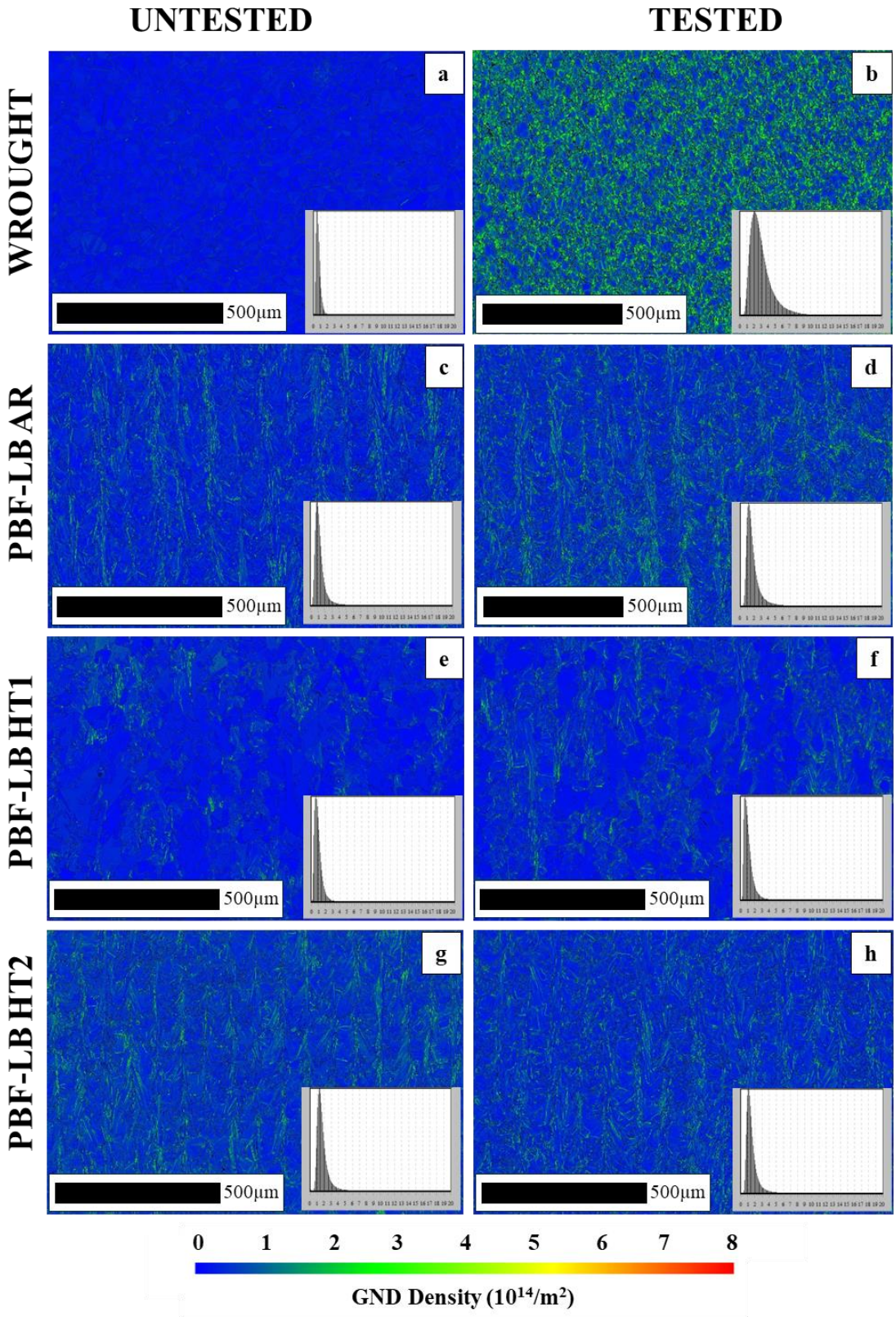

Figure 10. EBSD-derived GND density maps for wrought and PBF-LB IN718 in the untested and creep tested conditions at 650 °C and 650 MPa. All maps correspond to the X–Z plane (parallel to the loading direction).

Table 3: Data from EBSD IPFs map for wrought and PBF-LB IN718 before and after constant-load creep testing at 650 MPa, 650 °C.

Sample	With Twins			Twin Density (%)	Rx (%)	HAGBs (%)	LAGBs (%)	MOS (°)	GND Density ($10^{14}/m^{-2}$)
	Grain Area ($\mu m^{2)}$	Grain Diameter (µm)	Aspect Ratio						
Wrought Untested	193	12.5	0.49	51.4	97.9	93.0	7.0	1.15	0.68
Wrought Tested	43	6.2	0.56	4.88	25.6	23.0	77.0	4.5	2.98
AR Untested	195	10.4	0.42	0.5	29.7	49.2	50.8	2.6	1.39
AR Tested	151	9.1	0.44	0.6	26.3	45.2	54.8	3.6	1.77
HT1 Untested	293	13.3	0.47	25.3	77.1	60.6	39.4	1.9	0.98
HT1 Tested	291	13.4	0.47	13.8	67.2	53.8	46.2	2.7	1.14
HT2 Untested	174	9.8	0.43	0.3	34.0	36.0	64.0	2.7	1.77
HT2 Tested	167	9.7	0.44	0.6	30.7	49.0	51.0	3.15	1.58

3.4. DRX Pathways and Boundary Stability

A schematic illustration of DRX pathways relevant to IN718 during high-temperature deformation is shown in Figure 11. Discontinuous DRX (DDRX) involves the nucleation of new grains at existing grain boundaries, whereas continuous DRX (CDRX) proceeds via progressive subgrain rotation and boundary misorientation increase [14], [26].

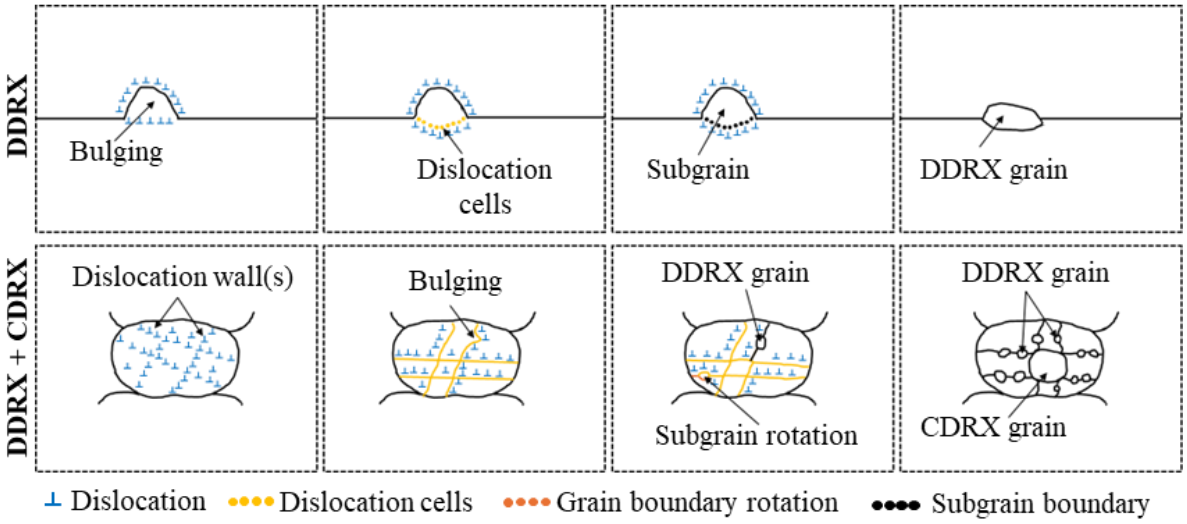

Figure 11. Schematic illustration of dynamic recrystallisation pathways relevant to IN718 during high-temperature deformation, showing discontinuous DRX (DDRX) and combined continuous–discontinuous DRX mechanisms. This schematic is intended as a conceptual aid rather than a direct reconstruction of the experimental microstructures.

The present results indicate that HT1 promotes a deformation-dominated DRX pathway, characterised by sustained GND accumulation and stable LAGB networks, whereas HT2 is biased toward recovery-dominated behaviour, with limited DRX activity and increased boundary mobility. As such, the findings demonstrate that the dominant DRX pathway during creep is not intrinsic to the alloy but is strongly influenced by the post-processing microstructural state. Deformation-dominated DRX, characterised by sustained dislocation storage and gradual boundary misorientation increase, promotes microstructural stability during creep. Recovery-dominated behaviour, by contrast, suppresses DRX activity and accelerates boundary instability. These differences have direct implications for creep stability, as discussed below.

3.5. Fractographic Observations

Post-creep fracture morphologies for wrought and PBF-LB IN718 variants are shown in Figure 12. Wrought IN718 exhibits predominantly ductile fracture features, including microvoid coalescence and limited intergranular cracking, consistent with its superior creep resistance [1–3]. The AR and HT2 conditions display extensive grain boundary cavitation and cavity coalescence, indicative of accelerated damage accumulation during creep. Such behaviour has been widely reported in additively manufactured IN718 and is commonly associated with unfavourable grain boundary character, residual segregation and continuous boundary phases [9], [19], [20]. In contrast, the HT1 condition exhibits a more dispersed cavitation morphology, with smaller and less interconnected cavities. This suggests improved resistance to grain boundary sliding and delayed onset of tertiary creep, consistent with the deformation-dominated DRX behaviour inferred from EBSD analysis. The observed fracture morphologies therefore provide further confirmation of the mechanistic distinctions drawn from microstructural characterisation [13], [15], [23].

The differences in fracture morphology between material conditions are consistent with the microstructural evolution observed by EBSD. The dispersed cavitation observed in wrought IN718 and

the HT1 condition suggests delayed grain boundary decohesion and enhanced resistance to cavity coalescence. In contrast, the extensive intergranular cavitation observed in the AR and HT2 conditions indicates premature grain boundary weakening and rapid damage accumulation. Such behaviour has been widely reported in additively manufactured IN718 and is commonly attributed to unstable grain boundary networks, residual segregation and recovery-dominated deformation during creep [9], [19], [20]. Likewise, the agreement between fracture observations and EBSD-derived deformation metrics supports the interpretation that DRX pathway plays a key role in governing creep damage evolution.

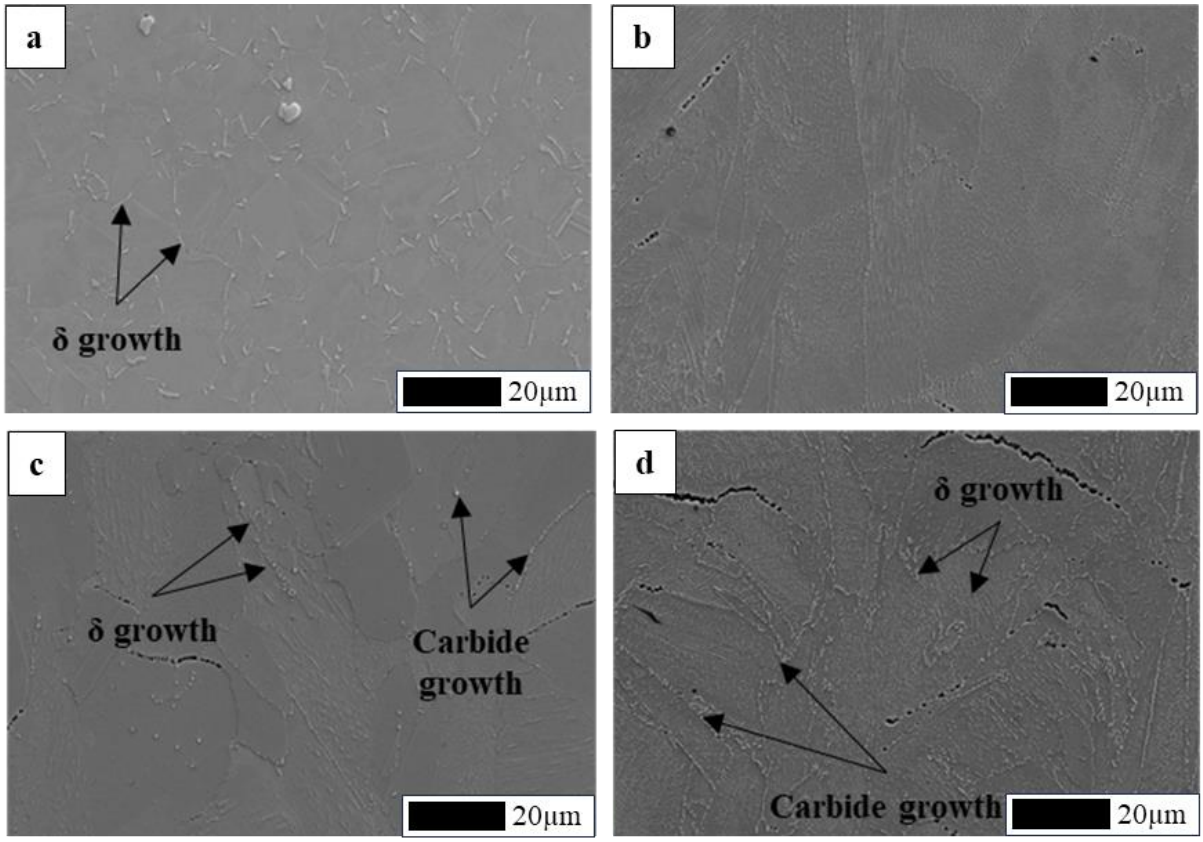

Figure 12. Post-creep FEG-SEM micrographs showing damage morphology in **a)** wrought IN718, **b)** PBF-LB AR, **c)** PBF-LB HT1 and **d)** PBF-LB HT2 IN718.

4. Discussion

The present results demonstrate that creep resistance in additively manufactured IN718 is governed by the stability of deformation-induced microstructures rather than grain size alone. While large equiaxed grains in wrought IN718 reduce the area available for grain boundary sliding, the comparable performance of the HT1 condition highlights the capacity of appropriately engineered PBF-LB microstructures to achieve similar stability through controlled dynamic recrystallisation behaviour [8], [11], [12].

The earlier onset of tertiary creep observed in the AR and HT2 conditions is interpreted as a consequence of boundary instability rather than simply increased dislocation mobility. In recovery-dominated microstructures, enhanced dislocation annihilation reduces internal back-stress and lattice curvature, diminishing the capacity for heterogeneous strain accommodation. This promotes grain boundary sliding and accelerates cavity nucleation at grain boundary precipitates and segregated regions. Once cavity density reaches a critical level, local stress concentration drives rapid strain-rate acceleration, marking the transition to tertiary creep.

In contrast, HT1 sustains geometrically necessary dislocation accumulation and stable low-angle boundary networks, which redistribute strain and delay boundary decohesion. As a result, tertiary creep onset is postponed despite comparable test temperature and stress conditions.

δ-phase precipitates also play a conditional role in this context. Discrete δ precipitates located at grain boundaries can contribute to boundary pinning and retard boundary migration, thereby supporting DRX stability and creep resistance. However, excessive or continuous δ networks promote Nb depletion of the matrix and weaken grain boundary cohesion, accelerating cavitation and intergranular fracture [23], [24], [29]. The HT1 condition resides within a narrow processing window in which δ-phase distribution supports creep stability, whereas HT2 exceeds this window, resulting in recovery-dominated behaviour and premature failure.

The EBSD-derived GND metrics provide quantitative evidence for contrasting deformation pathways. Deformation-dominated behaviour, characterised by sustained GND accumulation and stable LAGB networks, enhances creep resistance by accommodating strain while limiting boundary mobility. In contrast, recovery-dominated behaviour leads to GND annihilation, increased HAGB formation and accelerated damage accumulation. These trends are consistent with established DRX frameworks for IN718 and related superalloys [13], [14], [16], [26]. While increases in LAGB fraction and GND density with applied stress are consistent with dislocation-controlled creep and therefore not unexpected, the distinctive feature of the present study lies in the contrasting direction of microstructural evolution between post-processing conditions subjected to identical loading. Specifically, HT1 exhibits sustained GND accumulation alongside improved rupture life, whereas HT2 shows suppressed or reduced GND evolution despite inferior creep resistance. This divergence indicates that creep stability is governed not by the absolute magnitude of dislocation metrics, but by whether deformation proceeds through a deformation-dominated or recovery-dominated DRX pathway.

Post-processing heat treatments play a decisive role in biasing the material toward deformation-dominated or recovery-dominated creep behaviour. Deformation-dominated DRX promotes microstructural stability by sustaining dislocation substructures and limiting excessive boundary migration, thereby delaying damage accumulation. Conversely, recovery-dominated behaviour leads to dislocation annihilation, boundary coarsening and increased susceptibility to grain boundary sliding and cavitation. These results underscore the importance of treating creep as a microstructural evolution process and demonstrate the value of EBSD-derived metrics for identifying active deformation pathways in additively manufactured IN718.

Furthermore, the EBSD results presented here should not be interpreted as purely software-generated descriptors, but as physically meaningful indicators of the active deformation processes. For instance, GND density reflects lattice curvature required to accommodate plastic incompatibility between grains; LAGB networks represent evolving subgrain structures associated with continuous DRX; and changes in Σ3 boundary fraction indicate twin instability and boundary migration. Similarly, the role of δ-phase is conditional: discrete precipitates may contribute to boundary pinning, whereas excessive or continuous distributions promote intergranular weakening and cavitation. These interpretations provide a mechanistic link between microstructural evolution and tertiary creep onset. By interpreting these parameters within established creep and DRX frameworks, the analysis moves beyond microstructural description toward mechanistic understanding of how strain is accommodated and how boundary instability promotes tertiary creep.

5. Conclusions

This study has systematically examined the influence of additive manufacturing and post-processing heat treatment on the high-temperature creep behaviour and microstructural evolution of laser beam powder bed fusion (PBF-LB) IN718, with direct comparison to wrought material. The following conclusions can be drawn:

- Creep behaviour of PBF-LB IN718 at 625-675 °C and 625-690 MPa is governed by microstructural stability rather than grain size alone.

- A high-temperature solution plus double ageing treatment (HT1) yields creep resistance comparable to wrought IN718 by promoting deformation-dominated DRX and stable boundary networks.
- A lower-temperature heat treatment (HT2) exhibits recovery-dominated behaviour characterised by GND annihilation, high-angle boundary formation and accelerated creep damage.
- Twin boundary retention and controlled δ-phase distribution play supporting roles in stabilising creep-induced microstructures.
- Dynamic recrystallisation plays a central role in governing creep stability in IN718, with deformation-dominated DRX promoting sustained dislocation storage, stable boundary networks and improved resistance to creep damage accumulation.
- Post-processing heat treatments strongly bias the dominant DRX pathway during creep, with recovery-dominated behaviour leading to dislocation annihilation, boundary instability and accelerated failure, highlighting DRX control as a key lever in the microstructural design of IN718 for high-temperature service.

Acknowledgements

The current research was funded under the EPSRC Industrial Case Award EP/T517987/1. The provisions of research bursary, materials, and supporting information from ASTM AMCoE is gratefully acknowledged. Mechanical tests were performed at Swansea Materials Research and Testing Ltd. (SMaRT). Utilisation of the FEG-SEM was provided by Swansea University's Faculty of Science & Engineering Advanced Imaging of Materials (AIM) Facility, which was funded in part by the EPSRC (EP/M028267/1), The European Regional Development Fund through the Welsh Government (80708) and the Ser Solar project via the Welsh Government.

Data Availability

The raw/processed data required to reproduce these findings cannot be shared at this time as the data also forms part of an ongoing study.

Declaration of Competing Interest

The authors declare that they have no known competing financial interests or personal relationships that could have appeared to influence the work reported in this paper.

References

[1] Sames, W.J.; List, F.A.; Pannala, S.; Dehoff, R.R.; and Babu, S.S.; , "The metallurgy and processing science of metal additive manufacturing," *International Materials Reviews*, vol. 61, no. 5, pp. 315–360, Jul. 2016, doi: 10.1080/09506608.2015.1116649.

[2] DebRoy, T.; Wei, H.L.; Zuback, J.S.; Mukherjee, T.; Elmer, J.W.; Milewski, J.O.; Beese, A.M.; Wilson-Heid, A.; De, A.; and Zhang, W.; , "Additive manufacturing of metallic components – Process, structure and properties," *Prog. Mater. Sci.*, vol. 92, pp. 112–224, Mar. 2018, doi: 10.1016/j.pmatsci.2017.10.001.

[3] Amato, K.N.; Gaytan, S.M.; Murr, L.E.; Martinez, E.; Shindo, P.W.; Hernandez, J.; Collins, S.; and Medina, F.; , "Microstructures and mechanical behavior of Inconel 718 fabricated by selective laser melting," *Acta Mater.*, vol. 60, no. 5, pp. 2229–2239, 2012, doi: 10.1016/j.actamat.2011.12.032.

[4] Antonsson, T.; and Fredriksson, H.; , "The effect of cooling rate on the solidification of INCONEL 718," *Metallurgical and Materials Transactions B*, vol. 36, no. 1, pp. 85–96, Feb. 2005, doi: 10.1007/s11663-005-0009-0.

[5] Donachie, M.J.; and Donachie, S.J.; , *Superalloys: A Technical Guide*. ASM International, 2002.

[6] Sims, C.T.; Stoloff, N.S.; and Hagel, W.C.; , *Superalloys II*. Wiley, 1987.

[7] Reed, R.C.; , *The Superalloys: Fundamentals and Applications*. Cambridge University Press, 2006.

[8] Kuo, Y.-L.; Horikawa, S.; and Kakehi, K.; , “Effects of build direction and heat treatment on creep properties of Ni-base superalloy built up by additive manufacturing,” *Scr. Mater.*, vol. 129, pp. 74–78, Mar. 2017, doi: 10.1016/j.scriptamat.2016.10.035.

[9] Xu, Z.; Hyde, C.J.; Tuck, C.; and Clare, A.T.; , “Creep behaviour of inconel 718 processed by laser powder bed fusion,” *J. Mater. Process. Technol.*, vol. 256, pp. 13–24, Jun. 2018, doi: 10.1016/j.jmatprotec.2018.01.040.

[10] Tillmann, W.; Schaak, C.; Nellesen, J.; Schaper, M.; Aydinöz, M.E.; and Hoyer, K.-P.; , “Hot isostatic pressing of IN718 components manufactured by selective laser melting,” *Addit. Manuf.*, vol. 13, pp. 93–102, Jan. 2017, doi: 10.1016/j.addma.2016.11.006.

[11] Gallmeyer, T.G.; Moorthy, S.; Kappes, B.B.; Mills, M.J.; Amin-Ahmadi, B.; and Stebner, A.P.; , “Knowledge of process-structure-property relationships to engineer better heat treatments for laser powder bed fusion additive manufactured Inconel 718,” *Addit. Manuf.*, vol. 31, p. 100977, Jan. 2020, doi: 10.1016/j.addma.2019.100977.

[12] Shi, J.J.; Zhou, Z.Q.; Xu, K.; Zhou, G.Y.; Zhou, Z.J.; Li, C.P.; Chen, G.F.; Lu, X.G.; and Cao, G.H.; , “Effect of heat treatment on microstructure and small punch creep property of selective laser melted Inconel 718 alloy,” *Materials Science and Engineering: A*, vol. 853, p. 143748, Sep. 2022, doi: 10.1016/j.msea.2022.143748.

[13] Pradeep, K.; Buzolin, R.H.; Domankova, M.; Godor, F.; Stanojevic, A.; and Poletti, M.C.; , “Dynamic recrystallisation in Inconel®718 at creep conditions,” *Materials Science and Engineering: A*, vol. 893, p. 146146, Feb. 2024, doi: 10.1016/j.msea.2024.146146.

[14] Huang, K.; and Logé, R.E.; , “A review of dynamic recrystallization phenomena in metallic materials,” *Mater. Des.*, vol. 111, pp. 548–574, Dec. 2016, doi: 10.1016/j.matdes.2016.09.012.

[15] Hao, D.; Wang, Q.; Ma, H.; Wu, D.; Kang, J.; Dong, H.; You, B.; Li, N.; and Su, R.; , “The influence of grain boundary character distribution on the high-temperature creep behavior and damage mechanism of Inconel 718,” *Mater. Des.*, vol. 248, p. 113525, Dec. 2024, doi: 10.1016/j.matdes.2024.113525.

[16] Jiang, W.; Lu, J.; Guan, H.; Wang, M.; Cheng, X.; Liu, L.; Liu, X.; Wang, J.; Zhang, Y.; Zhang, Z.; Lin, W.; and Hu, J.; , “Study of pre-precipitated δ phase promoting deformation twinning and recrystallization behavior of Inconel 718 superalloy during hot compression,” *Mater. Des.*, vol. 226, p. 111693, Feb. 2023, doi: 10.1016/j.matdes.2023.111693.

[17] Bryndza, G.; Tchuindjang, J.T.; Chen, F.; Habraken, A.M.; Sepúlveda, H.; Tuninetti, V.; Mertens, A.; and Duchêne, L.; , “Review of the Microstructural Impact on Creep Mechanisms and Performance for Laser Powder Bed Fusion Inconel 718,” *Materials*, vol. 18, no. 2, p. 276, Jan. 2025, doi: 10.3390/ma18020276.

[18] Sabari, S.R.; Ilangovan, R.K.; Koundinya, N.T.B.N.; Amirthalingam, M.; Ram, G.D.J.; and Kottada, R.S.; , “Creep behaviour of additively manufactured nickel-based superalloys: a review,” *J. Mater. Sci.*, vol. 60, no. 39, pp. 18515–18548, Oct. 2025, doi: 10.1007/s10853-025-11359-7.

[19] Oros, T.J.; Son, K.; Hodge, A.M.; and Kassner, M.E.; , “The high temperature creep and fracture behavior of Inconel 718 produced by additive manufacturing,” *Scr. Mater.*, vol. 251, p. 116208, Oct. 2024, doi: 10.1016/j.scriptamat.2024.116208.

[20] Sabari, S.R.; Koundinya, N.T.B.N.; Godha, A.; Makineni, S.K.; Narayana Murty, S.V.S.; Nagesha, B.K.; Janaki Ram, G.D.; and Kottada, R.S.; , “Unravelling the dominant influence of microsegregation on creep rupture behaviour of additively manufactured inconel 718,” *Materials Science and Engineering: A*, vol. 919, p. 147480, Jan. 2025, doi: 10.1016/j.msea.2024.147480.

[21] Shi, J.J.; Zhou, S.A.; Chen, H.H.; Cao, G.H.; Russell, A.M.; Zhou, Z.J.; Qi, X.B.; Li, C.P.; and Chen, G.F.; , “Microstructure and creep anisotropy of Inconel 718 alloy processed by selective laser melting,” *Materials Science and Engineering: A*, vol. 805, p. 140583, Feb. 2021, doi: 10.1016/j.msea.2020.140583.

[22] Newell, D.J.; O’Hara, R.P.; Cobb, G.R.; Palazotto, A.N.; Kirka, M.M.; Burggraf, L.W.; and Hess, J.A.; , “Mitigation of scan strategy effects and material anisotropy through supersolvus annealing in LPBF IN718,” *Materials Science and Engineering: A*, vol. 764, p. 138230, Sep. 2019, doi: 10.1016/j.msea.2019.138230.

[23] Gao, Y.; Zhang, D.; Cao, M.; Chen, R.; Feng, Z.; Poprawe, R.; Schleifenbaum, J.H.; and Ziegler, S.; , "Effect of δ phase on high temperature mechanical performances of Inconel 718 fabricated with SLM process," *Materials Science and Engineering: A*, vol. 767, p. 138327, Nov. 2019, doi: 10.1016/j.msea.2019.138327.

[24] Chlebus, E.; Gruber, K.; Kuźnicka, B.; Kurzac, J.; and Kurzynowski, T.; , "Effect of heat treatment on the microstructure and mechanical properties of Inconel 718 processed by selective laser melting," *Materials Science and Engineering: A*, vol. 639, pp. 647–655, Jul. 2015, doi: 10.1016/j.msea.2015.05.035.

[25] ASTM International; , "ASTM E139-11: Standard Test Methods for Conducting Creep, Creep-Rupture, and Stress-Rupture Tests of Metallic Materials ," West Conshohocken, PA, 2018.

[26] Wang, Y.; Shao, W.Z.; Zhen, L.; Lin, L.; and Cui, Y.X.; , "Investigation on Dynamic Recrystallization Behavior in Hot Deformed Superalloy Inconel 718," *Materials Science Forum*, vol. 546–549, pp. 1297–1300, May 2007, doi: 10.4028/www.scientific.net/MSF.546-549.1297.

[27] May, P.E.; White, M.; Bordin, A.; Ednie, L.; Huff, R.; Vunnam, S.; Becker, L.; and Lancaster, R.J.; , "Influence of Heat Treatment on the High Temperature Properties of Inconel 718 Fabricated via Laser Beam Powder Bed Fusion," *Journal of Materials Research and Technology*, May 2025, doi: 10.1016/j.jmrt.2025.05.140.

[28] Frost, H.J.; and Ashby, M.F.; , *Deformation-Mechanism Maps*. Pergamon Press, 1982.

[29] Yuan, H.; and Liu, W.C.; , "Effect of the δ phase on the hot deformation behavior of Inconel 718," *Materials Science and Engineering: A*, vol. 408, no. 1–2, pp. 281–289, Nov. 2005, doi: 10.1016/j.msea.2005.08.126.